Development of a 6 DOF Soft Robotic Manipulator with Integrated Sensing Skin

Shen Treratanakulchai[1,2,3], Enrico Franco[2], Arnau Garriga-Casanovas[2], Hu Minghao[1], Panagiotis Kassanos[1], and Ferdinando Rodriguez y Baena[*,1,2]

***Abstract*— This paper presents a new 6 DOF soft robotic manipulator intended for colorectal surgery. The manipulator, based on a novel design that employs an inextensible tube to limit axial extension, is shown to maximize the force exerted at its tip and the bending angle, the latter being measured with a soft sensing skin. Manufacturing of the prototype is achieved with a lost-wax silicone-casting technique. The kinematic model of the manipulator, its workspace, and its manipulability are discussed. The prototype is evaluated with extensive experiments, including pressure-deflection measurement with and without tip load, and lateral force measurements with and without the soft sensing skin to assess hysteresis. The experimental results indicate that the prototype fulfils the key design requirements for colorectal surgery: (i) it can generate sufficient force to perform a range of laparoscopic tasks; (ii) the workspace is commensurate with the dimensions of the large intestine; (iii) the soft sensing skin only results in a marginal reduction of the maximum tip rotation within the range of pressures and external loads relevant for the chosen application.**

I. Introduction

Colon cancer was the third most common cancer in the world as reported in GLOBOCAN2020 [1]. Early detection and treatment are crucial for prevention and improved patient outcomes. However, conventional colonoscopy has several drawbacks, including discomfort and complications, which result in low uptake among patients. Thus, new laparoscopic instruments and corresponding workflows are needed to reduce patient discomfort, procedure time, and complications [2].

Soft robots are well suited for minimally invasive surgery (MIS), since they are intrinsically safe, they have no internal moving parts thus they can be miniaturised more easily, and their stiffness can be tuned in some cases. In addition, they can be manufactured with biocompatible materials, they can be safely disposed of after each surgery, and they can be compatible with magnetic resonance imaging (MRI). As a result, a myriad of soft robots has been proposed for MIS [3]. A notable example is stiff-flop, which has a tubular structure with multiple degrees-of-freedom (DOF) actuated with compressed air, which provides variable stiffness and some level of proprioceptive sensing [4], [5]. However, stiff-flop can only stiffen when stationary and the manipulator is comparatively large, which might be limiting for some endoscopic procedures. Another soft robot designed for MIS of the colon is described in [6]: the system has only two active DOF resulting in reduced mobility and limited ability to perform complex surgical tasks. Other examples that employ pneumatic artificial muscles arranged in parallel to generate bending include [7]–[9], as well as [10]–[15]. Several other soft robots, although not specifically designed for medicine, could be adapted for MIS, such as [16]–[18] and the flexible micro actuator (FMA) [19] , which in turn has inspired other similar designs [20].

Besides design, proprioceptive sensing is instrumental to performing complex manipulation tasks with soft robots that have multiple DOF [21]. To this end, Zhang et al. [22] developed a soft modular manipulator consisting of different sections stacked together with a magnetic interface. Subsequently, Truby et al. [23] used proprioceptive kirigami sensors and recursive neural networks to map the kinematics of three stacked soft actuators and to account for hysteresis and sensor nonlinearities. In summary, while several outstanding examples of soft manipulators have been proposed in the literature, to the best of our knowledge, none fully meets the requirements of colorectal surgery.

In this work, the design and development of a 6 DOF soft manipulator for colorectal surgery are presented. The design of the manipulator is optimized to achieve sufficient force for laparoscopic tasks despite its small size. The kinematics of the manipulator, its workspace and manipulability are discussed. The fabrication process, which employs a lost-wax silicone-casting technique, is outlined. The manipulator is integrated with a soft sensing skin that measures bending in a proprioceptive fashion. The prototype is evaluated with extensive experiments, including pressure-deflection measurements with tip load, and lateral force measurements with the sensing skin to quantify hysteresis.

II. Design and fabrication

A. Colon anatomy and design requirements

The large intestine has a complex shape consisting of five sections (i.e. rectum, sigmoid colon, descending colon, transverse colon, and ascending colon). The maximum diameters of the cecum, transverse colon, and descending colon are respectively 9 cm, 6 cm, and 3 cm [24]. Conventional

[1]The Hamlyn Centre for Robotic Surgery , Imperial College, London, United Kingdom. This research was supported by the Engineering and Physical Sciences Research Council (grant number EP/W004224/1).

[2]The Mechatronics in Medicine Laboratory, Imperial College, London, United Kingdom.

[3]Biomedical and Robotic Technology Laboratory, Mahidol University, Nakon Pathom, Thailand.

Email: [s.treratanakulchai17,f.rodriguez]@imperial.ac.uk

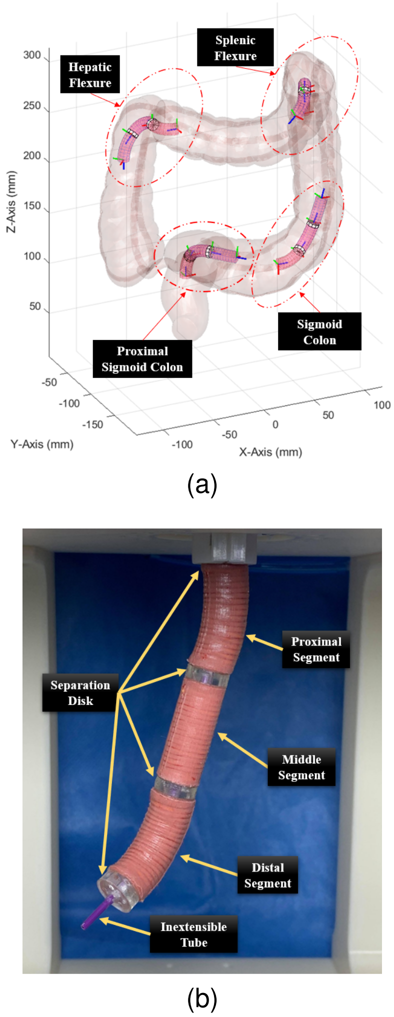

Fig. 1: (a) Schematic diagram of the colon with the proposed soft manipulator. (b) Prototype of the manipulator.

colonoscopes have an outer diameter ranging from 9.0 mm to 13.7 mm [25]. However, due to their limited number of DOF, navigating the intestine requires highly experienced operators. We hypothesize that mounting a soft manipulator with 6 DOF at the tip of a conventional colonoscope could mitigate these issues (see Figure 1a). Average tool forces for natural orifice transluminal endoscopic surgery (NOTEs) assessed during in-vivo tests on pigs are 0.8 N $\pm$ 0.7 N for pushing and pulling [26]. Thus, the soft manipulator should provide tip forces up to 1.5 N and bending angles larger than 90°.

B. Manipulator design

The prototype has a tubular geometry and consists of three actuated segments connected in series by rigid separation disks, which were aligned by means of a fixture, as shown in Figure 1b. Each actuated segment can bend in any direction, thus providing two actuated DOF. The three segments in series provide six actuated DOF at the distal end. The design of the actuated segments follows the framework presented in our previous work [27]. Firstly, to achieve bending on any plane, the segments have a uniform cross section divided into three equal chambers, which can be pressurized independently. The total cross-sectional area of the segments is maximized to increase the tip force, resulting in an 11.75 mm outer diameter, which meets the geometric requirements for colonoscopy. The three partition walls dividing the chambers were designed with minimum thickness and low stiffness to facilitate deformation of the cross-section when one or two chambers are pressurized. This enables the chambers to expand when pressurized, and thereby maximize the bending force. In addition, to facilitate bending, the internal chambers have a pleated structure which was obtained with a lost-wax process (see Section II-C).

An inextensible tube with a 1.47 mm inner diameter (5F Angiographic catheter, Merit Medical) was placed at the centre of the segments and was attached at both ends of each segment. This prevents axial elongation while enabling bending, thus increasing the bending force (see [27] for details). Moreover, the tube also serves as a working channel for feeding instruments (e.g. camera, laparoscopic tool, diagnostic probe, or laser ablation probe). Lastly, an inextensible thread (polyester thread, size 15, avg. break tensile force 7N) was wound around the outer surface of the prototype to prevent radial expansion, using a 1.25 mm pitch dual helix arrangement. The length of each segment is 25 mm and the separation disks are 3 mm thick, resulting in a total length of 84 mm for the prototype (see Section II-D).

Supply pipes connected to the chambers of the distal segments run inside the proximal and middle segments, resulting in a compact device. Therefore, the three segments have slightly different structures: the proximal segment has six passages for the supply pipes to the other two segments; the middle segment has three passages; the distal segment has no internal pipes. The supply pipes (Perfluoroalkoxy Polymer, IWASE Co.ltd, Japan) were inserted during the assembly procedure, and are characterized by small diameter (0.6 mm OD, a 0.4 mm ID), high pressure rating (5 bar maximum), bio-compatibility, and high chemical resistance. A soft sensing skin was mounted on the external surface of the prototype to measure the bending of the segments in a proprioceptive fashion (see Section III).

C. Fabrication process

The actuated segments were fabricated using lost-wax silicone casting which allows producing convex shapes with a small size. The fabrication process consists of four main steps: main body casting, fiber reinforcement, assembly, and sensor integration. A 3D printer (Objet500, Stratasys) was used to fabricate the molds required in the different steps.

The first step is the main body casting, which includes fabricating the wax cores corresponding to the internal chamber geometry, and the silicone casting. The inner chamber geometry of each segment was built by injecting molten wax into a first mold. The socket at both ends of the wax mold was used to align the chambers with the adjacent separation disks (see Figure 2a). We employed Paraffin wax (Materialix, Model No.49901), since it has a melting point

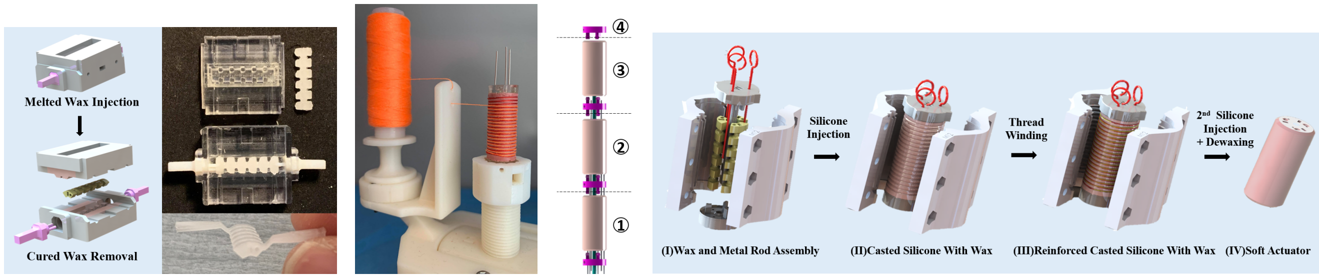

(a) (b) (c) (d)

Fig. 2: (a) Wax mould employed to fabricate the internal geometry of the chambers. (b) Custom 3D-printed thread winding station. (c) Sequence of assembly for the actuated segments. (d) Key steps in the fabrication process.

slightly above 56° Celsius hence it does not dissolve when curing the silicone. The wax cores were then assembled with two silicone molding caps and 0.7 mm metal rods used to create passages for the supply pipes (see Figure 2d). The number of metal rods varies depending on the segment, as discussed in Section II-B. The resulting mold was injected with silicone (Elastosil M4601, Wacker) and cured at 50° Celsius for 12 hours.

In the second step the silicone cast was reinforced by winding a double-helical inextensible polyester thread. The thread was wound into a groove on the cylindrical face of the silicone cast with a constant pitch of about 1.25 mm by employing a bespoke winding station (see Figure 2b). Afterwards, the resulting structure was covered with a thin layer (0.375 mm thickness) of silicone to fix the thread pitch to the groove. The wax inside the silicone mold was removed by rinsing with hot water, Toluene at 45 C° and finally with isopropanol. Once the cleaning process is completed, the weight of each actuated segment is approximately 2.5 grams.

In the third step three segments were connected in series to obtain a 6 DOF instrument. All components were bonded together with semi-flexible glue (i.e., polyolefin primer Permabond POP and flexible cyanoacrylate adhesive Permabond 2050, Permabond Engineering Adhesives Ltd, UK), which preserves some degree of viscosity, thus preventing cracks. The assembly sequence starts from the proximal segment and finishes with the distal segment, as shown in Figure 2c. Firstly, the central inextensible tube was glued to the proximal separation disk. At the same time, the supply pipes for the middle segment and the distal segment were inserted and glued into the proximal segment. Secondly, the supply pipes are inserted into the next separation disk, which was then glued to the proximal segment. These steps are then repeated for the remaining segments. Finally, a cap was mounted at the tip of the distal segment and attached to the inextensible tube. A leakage test was performed before integrating the soft sensing skin.

The last step in the fabrication process is sensing skin integration. PDMS material was used to cast the soft sensing skin, which features 9 sensing channels. The sensing skin was wrapped around the manipulator and glued to it with PDMS. Finally, all supply pipes were connected with a tapered syringe tip serving as adapter for the pneumatic actuation unit.

D. Kinematics and workspace

The kinematic analysis presented in this section relies on the constant curvature assumption (see Figure 3a), thus external loads are assumed negligible. The resulting kinematic model is characterized by two variables, namely the tip rotation on the bending plane ζ_i, and the orientation of the bending plane ϕ_i with respect to a fixed reference frame [28]. The curvature of a segment b_i and the arc length l_i are defined as

$$b_i = \frac{2\sin\zeta_i}{\sigma_i}, \tag{1}$$

$$l_i = \frac{\zeta_i \sigma_i}{\sin(\zeta_i)}. \tag{2}$$

Since the segments have constant axial length, the euclidean distance between tip and base is

$$\sigma_i = \frac{l_i \sin(\zeta_i)}{\zeta_i}. \tag{3}$$

When a segment is bending, the orientation of its tip is expressed in the ZYZ Euler angles convention by the homogeneous transformation matrix (4), which depends on σ_i, ζ_i, ϕ_i according to Rodrigues' formula.

$$T_i = \begin{bmatrix} S^2_{\phi_i}(1-C_{2\zeta_i})+C_{2\zeta_i} & S_{\phi_i}C_{\phi_i}(C_{2\zeta_i}-1) & C_{\phi_i}S_{2\zeta_i} & \sigma_i S_{\zeta_i}C_{\phi_i} \\ S_{\phi_i}C_{\phi_i}(C_{2\zeta_i}-1) & C^2_{\phi_i}(1-C_{2\zeta_i})+C_{2\zeta_i} & S_{\phi_i}S_{2\zeta_i} & \sigma_i S_{\zeta_i}S_{\phi_i} \\ -C_{\phi_i}S_{2\zeta_i} & -S_{\phi_i}S_{2\zeta_i} & C_{2\zeta_i} & \sigma_i C_{\zeta_i} \\ 0 & 0 & 0 & 1 \end{bmatrix} \tag{4}$$

The notation $C_{\phi_i} = \cos(\phi_i)$, $C_{\zeta_i} = \cos(\zeta_i)$, $S_{\phi_i} = \sin(\phi_i)$, $S_{\zeta_i} = \sin(\zeta_i)$ is employed here for conciseness. If instead the manipulator is straight (i.e. $\zeta_i = 0$), the corresponding transformation matrix represents a translation in z, that is

$$T_i = \begin{bmatrix} 1 & 0 & 0 & 0 \\ 0 & 1 & 0 & 0 \\ 0 & 0 & 1 & l_i \\ 0 & 0 & 0 & 1 \end{bmatrix}, \tag{5}$$

where l_i is the constant arc length, and also applies to the separation disk. The pose of the tip of the soft manipulator is

$$T^{base}_{tip} = T_1 T_d T_2 T_d T_3, \tag{6}$$

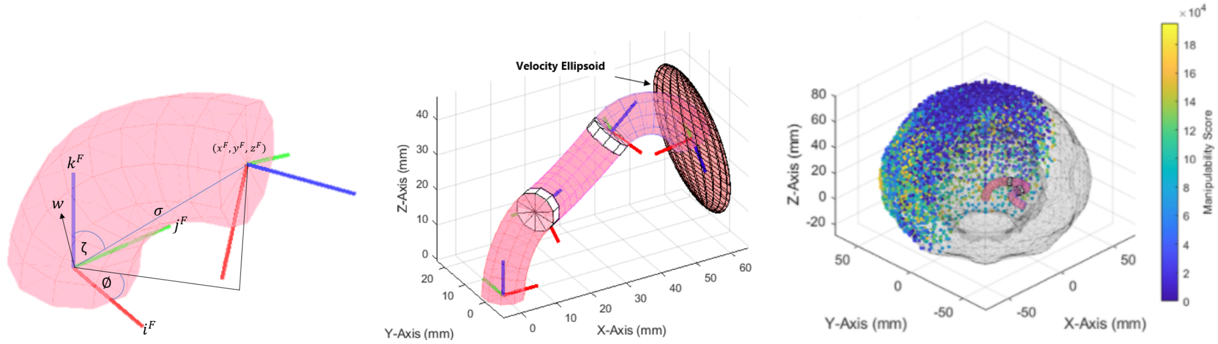

(a) (b) (c)

Fig. 3: Kinematic and workspace analysis: (a) Kinematic model of an actuated segment; (b) manipulability ellipsoid of the soft manipulator in one position; (c) reachable workspace and half of the dexterous workspace of the soft manipulator.

where T_1,T_2,T_3 are the transformation matrices of proximal segment, middle segment, and distal segment, while T_d refers to the separation disks.

The workspace of the soft manipulator is shown in Figure 3c, where the surface mesh represents the reachable workspace, while the scatter plot represents half of the dexterous workspace. For illustrative purposes, the angles ζ_i range from 0 to 45°, while ϕ_i range from 0 to 360°. The corresponding reachable workspace measures 71 mm in width and 81 mm in height, thus it can cover over 90% of the whole section of the cecum. A color bar shows the manipulability index, which is a measure of dexterity and is calculated as $M = \sqrt{JJ^T}$, where J is the Jacobian computed by differentiation of the tip pose with respect to ϕ_i and ζ_i, and it is given by

$$J_i = \begin{bmatrix} -\frac{lS_{\phi_i}S^2_{\zeta_i}}{\zeta_i} & -\frac{lC_{\phi_i}S_{\zeta_i}(S_{\zeta_i}-2\zeta C_{\zeta_i})}{\zeta_i^2} \\ \frac{lC_{\phi_i}S^2_{\zeta_i}}{\zeta_i} & -\frac{lS_{\phi_i}S_{\zeta_i}(S_{\zeta_i}-2\zeta C_{\zeta_i})}{\zeta_i^2} \\ 0 & -\frac{l(S_{2\zeta_i}-2\zeta_i C_{2\zeta_i})}{2\zeta_i} \end{bmatrix}. \quad (7)$$

The manipulability ellipsoid, which represents the ability of the manipulator to change the orientation of the tip at each location, is shown in Figure 3b. It follows from (7) that the angle ϕ does not affect M on the z axis. Finally, if $\zeta_i = 0$ (i.e. the segments are straight), the Jacobian is undefined.

III. SENSING SKIN

The sensing skin should have similar mechanical properties to the manipulator to allow unhindered motion. A wide range of materials, fabrication methods, sensing modalities, and architectures can be used for strain/pressure sensing in soft manipulators [29] including capacitive, inductive, impedimetric, piezoelectric, optical, and piezoresistive principle, with the latter being the most common modality. While high-cost microfabrication is often used to create intricate high-resolution devices, we employed a clean-room free, lower-cost additive fabrication approach [30].

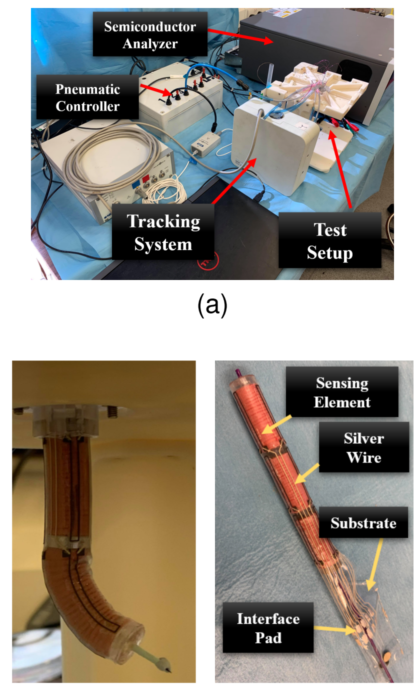

(a)

(b) (c)

Fig. 4: (a) Experiment setup; (b) bent manipulator with sensing skin; (c) components of sensing skin

In particular, a piezoresistive sensing skin consisting of three strain sensing elements at each primary bending direction for each of the three segments of the soft manipulator was designed. Thus, a 3 x 3 sensor array was fabricated on a 0.3 mm thick polydimethylsiloxane (PDMS, Sylgard 184, Dow Cornig, USA) substrate. A 10:1 prepolymer to curing agent weight ratio was used. Custom conductive elastomeric composites of PDMS with graphite powder and with silver microparticles were used. The piezoresistive sensing elements were printed using a graphite-PDMS composite ink, while the silver-PDMS composite was used to print the electrical interconnects. The latter is significantly less piezoresistive, thus the resistance change of the graphite composites will dominate a two-point resistance measurement. This consequently reduces the need for bonding pads, facilitating the integration with the soft manipulator. Three stainless steel stencil masks with a thickness of 0.1 μm were designed: one for the strain sensing elements, one for the electrical interconnects, and a final one for the bonding pads used for interfacing the skin to the electronic instrumentation. The bonding pads, which were located at the bottom of the sensing skin as shown in Figure 4c, were printed with the graphite-PDMS ink, as their conductivity is not critical, and it were then covered with silver paste (RS Components, UK) to attach 27 AWG wires. Subsequently, the device was degassed for 15 minutes and then baked for 2 hours at 70 °C. After the wires were attached with the silver paste, the device was again baked at 140 °C for 10 minutes to cure the paste. Square graphite-PDMS pads were added at each terminal of the piezoresistive sensing elements of the skin to ensure that an electrical connection is achieved with the printed silver-PDMS interconnects. For the graphite-PDMS ink, a weight ratio of 24% was used. This choice was based on the work presented in [30] to achieve a good trade-off between mechanical properties, hysteresis, linearity, and stain-sensing characteristics of the material. For the silver-PDMS composite, a 70% weight ratio was empirically chosen to achieve good mechanical and electrical properties, low stain sensitivity, and an ink viscosity suitable for stencil printing (see [30] for more details on the formulation, processing, and printing of the inks). Custom 3D printed molds and fixtures were used to produce a 0.3 mm thick PDMS substrate and to align the three masks. The sensing skin is shown in Figure 4.

IV. EXPERIMENTAL RESULTS

Experiments were conducted to assess the performance of the soft manipulator. The tip rotation was measured at different pressures of the internal chambers, and the measurements were repeated without the soft sensing skin and with different sensing skin thicknesses (i.e. 0.3mm, 0.5 mm, 0.75 mm). The measurements were then repeated in the presence of external tip forces to assess hysteresis. The lateral force at the tip of the manipulator was then measured at different pressures. Finally, the resistance of the sensing elements on the sensing skin was measured at different bending angles corresponding to increasing pressures.

A. Measurement of the bending angle

The position and orientation of the tip of the manipulator were measured with an electromagnetic (EM) tracking system (Aurora, NDI) and one EM sensor was attached at the tip of the manipulator. The pressure in the internal chambers was measured with a pressure sensor (MXP2022, NXP). The system setup is shown in Figure 4a: the manipulator is clamped at the base and hangs down vertically at rest as shown in Figure 1b. This configuration, although not representative of the application, is widely used for the mechanical characterization of soft manipulators. The actuated segment was pressurized independently by employing proportional valves (Tecno Basic, Hoerbiger). A Matlab script was employed to communicate the pressure values to the valves though a microcontroller (mbed NXP LPC1768) with a Remote Procedure Call protocol. The maximum pressure was limited to 3 bar for safety.

The chambers of each segment were supplied with increasing pressure values while recording the tip orientation. The pressure was increased in 10 steps from 0 to 3 bar with a 10 s time interval to allow the system to stabilize. After reaching the maximum, the pressure was instantly released to assess hysteresis in a worst case scenario. The measurements were repeated 5 times for this setup. The results show in Figure 5a, indicated that the three actuated segments behave slightly differently. This is expected since the proximal segments support the additional weight of the distal segments. The average bending angle and orientation of the bending plane at 3 bar for the proximal, middle, and distal segment considering sensing skins of different thicknesses are listed in Table I. The results indicate that adding the soft sensing skin slightly reduces the bending angle at a given pressure and it slightly varies the orientation of the bending plane. The results also suggest that the relationships between bending angle ζ_i, orientation of the bending plane ϕ_i, and pressure are nonlinear , similarly to our previous prototypes [31].

Figure 5b shows the tip position of each actuated segment when pressurized and highlights the effect of the soft sensing skin. Hysteresis was assessed by measuring the Euclidean distance between the tip position at rest and after applying and removing pressure (see Table I). The last column of Table I shows that the additional stiffness resulting from the sensing skin can partially overcome hysteretic effects arising from the inextensible tube at the center of the

TABLE I: Experimental results

Segment	Bending angle at 3 Bar (rad)				Bending plane orientation at 3 Bar (rad)				Euclidean Distance (mm)			
	No Skin	0.3 mm	0.5 mm	0.75 mm	No Skin	0.3 mm	0.5 mm	0.75 mm	No Skin	0.3 mm	0.5 mm	0.75 mm
1	0.6707	0.51	0.507	0.4507	-0.2759	-0.1796	-0.3034	-0.0482	3.4546	4.4122	3.5416	1.5392
2	1.5763	1.412	1.1739	0.9674	-0.6265	-0.4956	-0.6091	-0.3474	2.4102	1.7665	1.9562	1.1455
3	1.7233	1.593	1.2177	1.2684	-0.5813	-0.5239	-0.4333	-0.5343	0.8099	0.6966	0.4883	0.5838

Segment	Tip Position on vertical axis (mm)		Potential Energy (J)			
	No Load	20 g Load	No Load	20 g Load	Energy Difference	Percentage Change(%)
1	-92.0369	-40.2239	-7.88	-18.039	10.159	-128.92%
2	-82.2772	-51.22	-10.03912	-16.1263	6.08718	-60.63%
3	-47.6822	-42.5273	-8.3353	-9.3457	1.0104	-12.12%

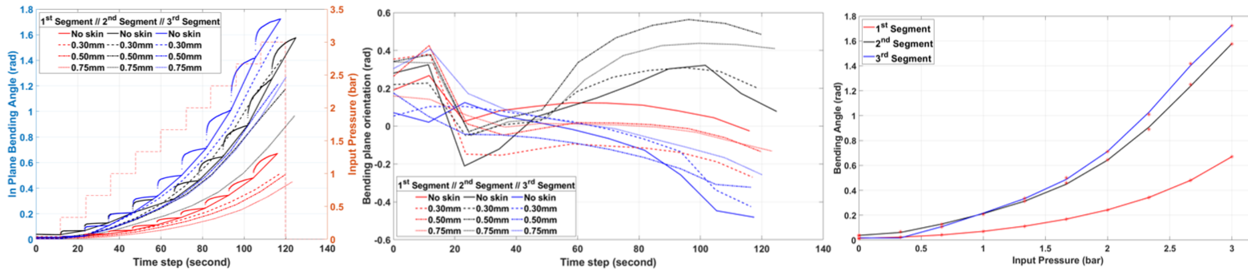

(a)

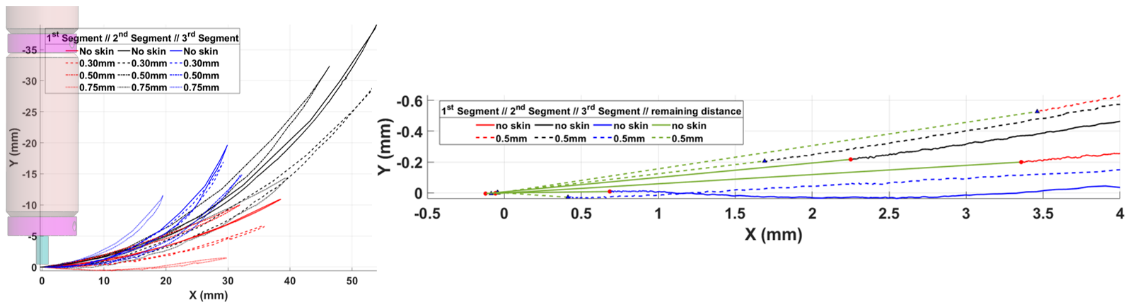

(b)

Fig. 5: (a) Bending angle at different pressures (left); orientation of the bending plane at different pressures (centre); relationship between bending angle and pressure (right). (b) Tip position of the manipulator (left); detail view of the origin (right).

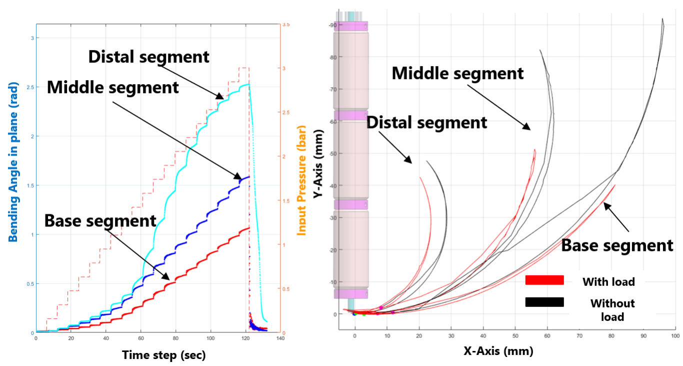

(a)

(b)

Fig. 6: (a) Bending angles of the actuated segments with a 20 g mass attached at the tip of the manipulator (left); tip position with and without tip mass (right). (b) Test setup with 20 g mass attached at the tip of the manipulator.

manipulator. Thus we can infer from the results that complete cancellation of hysteretic effects could be achieved with a non-uniform thickness of the sensing skin at the cost of reducing the maximum bending angle and the maximum lateral force. Manufacturing a variable-thickness sensing skin requires significant changes to the current process and shall be investigated in our future work.

B. Effect of external forces

To assess the effect of an external force on the bending angles, a 20 g mass was attached at the tip of the manipulator (see Figure 6b). The resulting moment acts on the proximal segment and attempts to align the manipulator with gravity. The position on the vertical axis is employed to compute the potential energy of the tip mass, while the tip rotations are compared to the values without the tip mass (see Figure 6a). The results are summarized in Table I.

C. Lateral Force Measurement

The lateral force produced by one actuated segment was measured with an electronic scale, as shown in Figure 7. Two conditions were considered: in the first one, the pressure was increased up to 2 bar in one chamber, while the remaining chambers were left at atmospheric pressure. In the second condition, two chambers were supplied at constant pressure (i.e., 0.2 bar) to prevent twisting effects, while the remaining chamber was pressurized up to 3 bar. The maximum lateral force was 1.56 N in the first case and 1.99 N in the second,

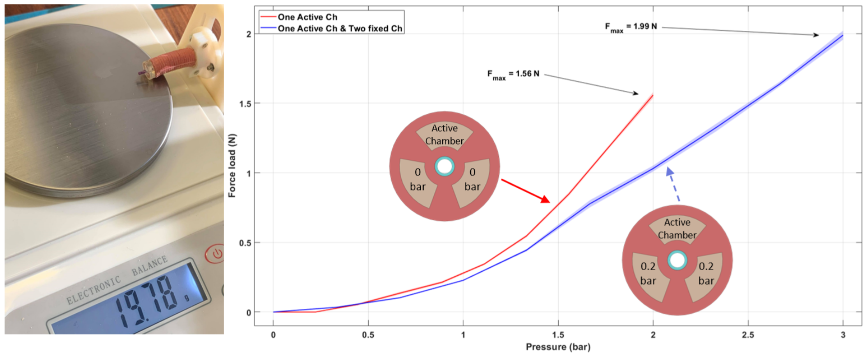

Fig. 7: Lateral force measurement for one actuated segment: test setup (left); force measurements (right).

which is larger than the average forces for push / pull tasks in NOTES [26].

D. Sensing skin measurements

The resistance of the sensing skin at increasing pressures of the actuated segments was recorded with a semiconductor analyzer (4200A-SCS, Keithley) using standard two-point measurements. The experiment was repeated 5 times for each segment.Figure 8c shows the filtered value of the resistance of actuated segment, which increases simultaneously to the pressure. In Figures 8b and 8d, the raw resistance was averaged over all data points and over the five trials, and then normalized, showing that there is a 1 to 1 correspondence between resistance and bending angle. This suggests that the sensing skin could be used to measure the bending angle in a proprioceptive fashion by employing appropriate signal processing and calibration techniques, which will be investigated in future work.

V. CONCLUSION

This paper presented the design and fabrication of a 6 DOF soft continuum manipulator consisting of three actuated segments connected in series. The fabrication of the prototype employs a lost-wax casting technique. A simplified kinematic model was employed to analyze the workspace of the manipulator and the manipulability index. Finally, the working principle of the soft sensing skin and its integration with the manipulator were described in detail.

Experiments were conducted to characterize and evaluate the prototype. The results indicate that the manipulator has nonlinear stiffness, which is in accordance with our earlier works. In addition, the three actuated segments have different stiffness characteristics due to their different internal structure. The soft sensing skin helps reducing hysteresis and only results in a small reduction of the bending angle. Thanks to a unique design based on an inextensible tube that limits axial extension of the soft manipulator, the system was shown to provide sufficient bending angle and force output for a range

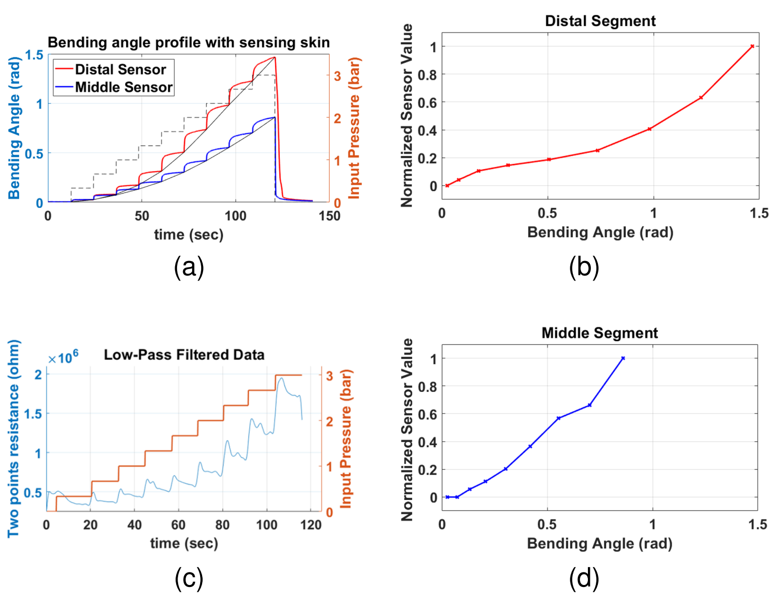

Fig. 8: (a) Bending angle of distal/middle segment with sensing skin; (b,d) relationship between bending angle and normalized resistance value for distal segment and middle segment; (c) 0.5 Hz Low-pass filter resistance for stepped input pressure.

of minimally invasive tasks. Finally, the results show that the sensing skin can be used to measure the bending angle of different segments, thus it could eventually replace external EM sensors.

Future work shall focus on minimizing hysteresis and on further improving the fabrication process in order to reduce offset between segments, which could lead to undesired twist. In addition, an analytical model of the stiffness of the manipulator will be constructed, and signal processing techniques will be employed to reconstruct the bending angles from the measurements of the sensing skin. Finally, we intend to integrate the soft manipulator with an endoscope resulting in a complete system for MIS of the large intestine.

ACKNOWLEDGMENTS

The first author is grateful to Meysam Keshavarz for his guidance on mould design and material selection, and to Dominic J Wales for his advice on dewaxing methods. This work is partially supported by a research collaboration with the Multi-Scale Medical Robotics Centre, The Chinese University of Hong Kong.

REFERENCES

[1] H. Sung, J. Ferlay, R. L. Siegel, M. Laversanne, I. Soerjomataram, A. Jemal, and F. Bray, "Global cancer statistics 2020: Globocan estimates of incidence and mortality worldwide for 36 cancers in 185 countries," *CA: A Cancer Journal for Clinicians*, vol. 71, no. 3, pp. 209–249, 2021.

[2] G. Ciuti, K. Skonieczna-Żydecka, W. Marlicz, V. Iacovacci, H. Liu, D. Stoyanov, A. Arezzo, M. Chiurazzi, E. Toth, H. Thorlacius, P. Dario, and A. Koulaouzidis, "Frontiers of robotic colonoscopy: A comprehensive review of robotic colonoscopes and technologies," *Journal of Clinical Medicine*, vol. 9, no. 6, 2020.

[3] A. De Greef, P. Lambert, and A. Delchambre, "Towards flexible medical instruments: Review of flexible fluidic actuators," *Precision Engineering*, vol. 33, no. 4, pp. 311–321, 2009.

[4] M. Cianchetti, T. Nanayakkara, T. Ranzani, G. Gerboni, K. Althoefer, P. Dasgupta, and A. Menciassi, "Soft Robotics Technologies to Address Shortcomings in Today's Minimally Invasive Surgery: The STIFF-FLOP Approach," *Soft Robotics*, vol. 1, no. 2, pp. 122–131, 2014.

[5] J. Czarnowski, M. Macia, J. Główka, M. Cianchetti, and A. Menciassi, "New STIFF-FLOP module construction idea for improved actuation and sensing," in *IEEE International Conference on Robotics and Automation (ICRA)*, 2015, pp. 2901–2906.

[6] G. Chen, M. T. Pham, T. Maalej, H. Fourati, R. Moreau, and S. Sesmat, "A Biomimetic steering robot for Minimally invasive surgery application," *IN-TECH*, 2009.

[7] G. Smoljkic, G. Borghesan, D. Reynaerts, J. D. Schutter, J. V. Sloten, and E. V. Poorten, "Hybrid robotic system for applications in robotic surgery," *Proceedings of the 5th Joint Workshop on New Technologies for Computer/Robot Assisted Surgery*, pp. 1–3, 2015.

[8] A. Devreker, B. Rosa, A. Desjardins, E. J. Alles, L. C. Garcia-Peraza, E. Maneas, D. Stoyanov, A. L. David, T. Vercauteren, J. Deprest, S. Ourselin, D. Reynaerts, and E. Vander Poorten, "Fluidic actuation for intra-operative in situ imaging," in *IEEE International Conference on Intelligent Robots and Systems*, vol. 2015-Decem, 2015, pp. 1415–1421.

[9] G. Smoljkic, G. Borghesan, A. Devreker, E. V. Poorten, B. Rosa, H. De Praetere, J. De Schutter, D. Reynaerts, and J. V. Sloten, "Control of a hybrid robotic system for computer-assisted interventions in dynamic environments," *International Journal of Computer Assisted Radiology and Surgery*, vol. 11, no. 7, pp. 1371–1383, 2016.

[10] W. McMahan, V. Chitrakaran, M. Csencsits, D. Dawson, I. D. Walker, B. Jones, M. Pritts, D. Dienno, M. Grissom, and C. D. Rahn, "Field trials and testing of the OcotArm continuum manipulator," in *IEEE international conference on robotics and automation (ICRA)*, 2006.

[11] I. D. Walker, D. M. Dawson, T. Flash, F. W. Grasso, R. T. Hanlon, B. Hochner, W. M. Kier, C. C. Pagano, C. D. Rahn, and Q. M. Zhang, "Continuum robot arms inspired by cephalopods," *SPIE Conference on Unmanned Ground Vehicle Technology*, vol. 5804, pp. 303–314, 2005.

[12] N. Giri and I. D. Walker, "Three module lumped element model of a continuum arm section," in *IEEE International Conference on Intelligent Robots and Systems (IROS)*, San Francisco, CA, USA, September 25-30, 2011, pp. 4060–4065.

[13] I. S. Godage, G. A. Medrano-Cerda, D. T. Branson, E. Guglielmino, and D. G. Caldwell, "Dynamics for variable length multisection continuum arms," *International Journal of Robotics Research*, vol. 35, no. 6, pp. 695–722, 2015.

[14] I. S. Godage and I. D. Walker, "Dual Quaternion based modal kinematics for multisection continuum arms," *Proceedings - IEEE International Conference on Robotics and Automation*, vol. 2015-June, no. June, pp. 1416–1422, 2015.

[15] I. S. Godage, R. Wirz, I. D. Walker, and R. J. Webster, "Accurate and Efficient Dynamics for Variable-Length Continuum Arms: A Center of Gravity Approach," *Soft Robotics*, vol. 2, no. 3, pp. 96–106, 2015.

[16] D. Trivedi, C. D. Rahn, W. M. Kierb, and I. D.Walkerc, "Soft robotics: Biological inspiration, state of the art, and future research," *Applied Bionics and Biomechanics*, 2008.

[17] D. Rus and M. T. Tolley, "Design, fabrication and control of soft robots," *Nature*, vol. 521, no. 7553, pp. 467–475, 2015.

[18] J. Bishop-Moser, G. Krishnan, C. Kim, and S. Kota, "Design of soft robotic actuators using fluid-filled fiber-reinforced elastomeric enclosures in parallel combinations," in *IEEE International Conference on Intelligent Robots and Systems (IROS)*, 2012.

[19] K. Suzumori, S. Iikura, and H. Tanaka, "Development of flexible microactuator and its applications to robotic mechanisms," in *IEEE International Conference on Robotics and Automation (ICRA)*, 1991.

[20] R. Abe, K. Takemura, K. Edamura, and S. Yokota, "Concept of a micro finger using electro-conjugate fluid and fabrication of a large model prototype," *Sensors and Actuators, A: Physical*, 2007.

[21] M. Runciman, A. Darzi, and G. P. Mylonas, "Soft robotics in minimally invasive surgery," *Soft Robot*, vol. 6, no. 4, pp. 423–443, 2019.

[22] B. Zhang, C. Hu, P. Yang, Z. Liao, and H. Liao, "Design and modularization of multi-dof soft robotic actuators," *IEEE Robotics and Automation Letters*, vol. 4, no. 3, pp. 2645–2652, 2019.

[23] R. L. Truby, C. Della Santina, and D. Rus, "Distributed proprioception of 3d configuration in soft, sensorized robots via deep learning," *Ieee Robotics and Automation Letters*, vol. 5, no. 2, pp. 3299–3306, 2020.

[24] J. R. Monson and C. Macklin, "Colonoscopy," *Diseases of the Colon and Rectum*, vol. 49, no. 11, pp. 1794–1796, feb 2006.

[25] A. J. Trindade, D. R. Lichtenstein, H. R. Aslanian, M. S. Bhutani, A. Goodman, J. Melson, U. Navaneethan, R. Pannala, M. A. Parsi, A. Sethi, S. Sullivan, N. Thosani, G. Trikudanathan, R. R. Watson, and J. T. Maple, "Devices and methods to improve colonoscopy completion (with videos)," *Gastrointestinal Endoscopy*, vol. 87, no. 3, pp. 625–634, 2018.

[26] A. L. Trejos, S. Jayaraman, R. V. Patel, M. D. Naish, and C. M. Schlachta, "Force sensing in natural orifice transluminal endoscopic surgery," *Surgical Endoscopy*, vol. 25, no. 1, pp. 186–192, jun 2011.

[27] A. Garriga-Casanovas, I. Collison, and Y. B. F. Rodriguez, "Toward a common framework for the design of soft robotic manipulators with fluidic actuation," *Soft Robot*, vol. 5, no. 5, pp. 622–649, 2018.

[28] A. Garriga-Casanovas and F. Rodriguez y Baena, "Kinematics of continuum robots with constant curvature bending and extension capabilities," *Journal of Mechanisms and Robotics*, vol. 11, no. 1, 2019.

[29] P. Kassanos, S. Anastasova, C. M. Chen, and G. Z. Yang, "Sensor embodiment and flexible electronics," in *Implantable Sensors and Systems: From Theory to Practice*. Springer International Publishing, jan 2018, pp. 197–279.

[30] M. Hu, P. Kassanos, M. Keshavarz, E. Yeatman, and B. Lo, "Electrical and mechanical characterization of carbon-based elastomeric composites for printed sensors and electronics." Institute of Electrical and Electronics Engineers (IEEE), jul 2021, pp. 1–4.

[31] E. Franco, A. Garriga-Casanovas, J. Tang, F. Rodriguez y Baena, and A. Astolfi, "Adaptive energy shaping control of a class of nonlinear soft continuum manipulators," *IEEE ASME Trans Mechatron*, pp. 1–11, 2021.